Morphological Evolution of Carbon Nanofibers Encapsulating SnCo Alloys and Its Effect on Growth of the Solid Electrolyte Interphase Layer

Jungwoo Shin,[†] Won-Hee Ryu,[†] Kyu-Sung Park,[‡] and Il-Doo Kim[†,*]

[†]Department of Materials Science and Engineering, Korea Advanced Institute of Science and Technology, 291 Daehak-ro, Yuseong-gu, Daejeon 305-701, Republic of Korea and [‡]Texas Materials Institute, The University of Texas at Austin, Austin, Texas 78712, United States

ABSTRACT Two distinctive one-dimensional (1-D) carbon nanofibers (CNFs) encapsulating irregularly and homogeneously segregated SnCo nanoparticles were synthesized *via* electrospinning of polyvinylpyrrolidone (PVP) and polyacrylonitrile (PAN) polymers containing Sn—Co acetate precursors and subsequent calcination in reducing atmosphere. CNFs synthesized with PVP, which undergoes structural degradation of the polymer during carbonization processes, exhibited irregular segregation of heterogeneous alloy particles composed of SnCo, Co_3Sn_2, and SnO with a size distribution of 30—100 nm. Large and exposed multiphase SnCo particles in PVP-driven amorphous CNFs (SnCo/PVP-CNFs) kept decomposing liquid electrolyte and were partly detached from CNFs during cycling, leading to a capacity fading at the earlier cycles. The closer study of solid electrolyte interphase (SEI) layers formed on the CNFs reveals that the gradual growth of fiber radius due to continuous increment of SEI layer thickness led to capacity fading. In contrast, SnCo particles in PAN-driven CNFs (SnCo/PAN-CNFs) showed dramatically reduced crystallite sizes (<10 nm) of single phase SnCo nanoparticles which were entirely embedded in dense, semicrystalline, and highly conducting 1-D carbon matrix. The growth of SEI layer was limited and saturated during cycling. As a result, SnCo/PAN-CNFs showed much improved cyclability (97.9% capacity retention) and lower SEI layer thickness (86 nm) after 100 cycles compared to SnCo/PVP-CNFs (capacity retention, 71.9%; SEI layer thickness, 593 nm). This work verifies that the thermal behavior of carbon precursor is highly responsible for the growth mechanism of SEI layer accompanied with particles detachment and cyclability of alloy particle embedded CNFs.

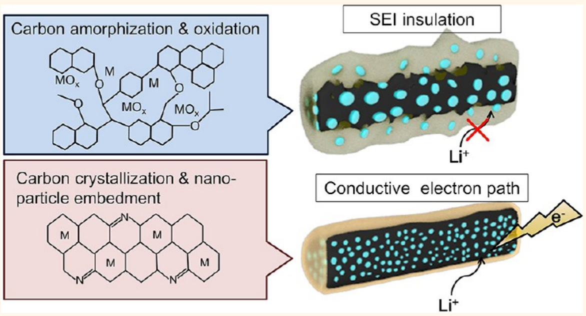

KEYWORDS: Li-ion batteries · tin alloy · anode · carbon nanofiber · solid electrolyte interphase

One of the great interests in the study of Li-ion batteries is securing anode materials that possess high capacity, high power, and excellent cyclability.[1] Metallic tin (Sn) has been suggested as a prospective substitute for the conventional graphite anode (372 mAh/g) due to its high theoretical capacity (992 mAh/g) and thermal stability.[2] However, it has been shown to be difficult to utilize pure Sn due to its large specific volume changes (<300%) during cycling that accompany alloying/dealloying with lithium. The volume change can cause pulverization of electrode materials and loss of electrical contact between active material and carbon/current collector, thereby continuously losing capacity as the cycle progresses.[3]

So far, factors affecting the performance of Sn-based anode are categorized according to the particle size and the presence of alloy elements and/or carbon. The idea generally accepted for improving Sn-based anode materials is to decrease the particle size so as to abate the absolute volume expansion.[4] Alloying with electrochemically inactive materials can also provide a buffer phase to relieve the stress arising from the volume changes.[5] Among various transition metals including Ni,[6,7] Sb,[8] Cu,[9] Ag,[10] and Co,[11] Co prevents the formation of carbide phases such as CoC_x.[12] Because the direct formation of the solid electrolyte interphase (SEI) film onto the surface of metallic anode can lead to surface crack as well as repeated regeneration of the SEI layers, carbon

* Address correspondence to idkim@kaist.ac.kr.

Received for review June 13, 2013 and accepted July 16, 2013.

10.1021/nn403003b

coating has also been suggested as a promising solution to prevent the surface pulverization.[13−16]

Besides the issues stated above, the dynamic formation and electrochemical stability of solid electrolyte interphase (SEI) layer on the surface of electrode materials is also an important issue for the Sn-based anode materials. The SEI layers are generally formed *via* the reductive decomposition of organic solvent and electrolyte additives,[17] if the anode electrochemical potential is above the lowest unoccupied molecular orbitals (LUMO). If severe volume changes take place, for instance, in metallic anode materials with 300% of volume expansion ratio compared to their original occupied space, the SEI layers can be damaged or even broken during the charge/discharge cycles.[18] Therefore, during subsequent electrochemical reactions, the SEI layers are repeatedly regenerated, thereby increasing the SEI thickness and their electrical resistance. Since SEI layers are composed of multilayers of organic and inorganic compounds such as Li_2CO_3 and Li_2O,[19] irreversible capacity loss caused by encapsulation of the insulating SEI film on separated anode particles can be a major problem as well. One more issue, which should be considered from the dynamic formation of the SEI layers, is that it continuously robs lithium ions from cathode, so the SEI layers make the capacity of a full cell faded. Therefore, forming the thin SEI layer and maintaining the stable SEI layers are the key issues to improve the electrochemical performance.

In addition to those factors influencing anode properties, we focused on establishing the morphological impact of Sn-based anode on securing both optimum capacity and cyclability . Of the various morphologies designed to avoid those issues, one-dimensional (1-D) electrospun carbon coated structure have drawn great attention because it is the simplest one-step synthetic method to prepare alloy nanoparticles within 1-D uniform carbon coating, which assist the formation of the SEI layers on the ion-conducting carbon shield.[20] The morphological advantage of 1-D carbon coated structure is the open space between each 1-D structures that accommodate large strain without pulverization[21] and the charge-transport directionality that shows the electronic conduction along the axial direction associated with the Li^+-ion diffusion mainly along the short radial direction. Unlike 0-D or irregular structures,[22] the interfacial Li^+-ion transfer takes place on the 1-D cylindrical surface which is exposed to the electrolyte, thereby resulting in radial formation of the SEI layers. Furthermore, the continuous electron conduction path along the axial direction can minimize the irreversible capacity loss caused by isolation of active materials.

However, the studies of the carbon coated 1-D anodes have seldom focused on its unique dynamic behavior when exposed to electrolytes during cell operation. Gradual growth of SEI layer can reduce electrolyte channel spaces between carbon nanofibers (CNFs) and impede Li^+-ion charge transfer through the thicker SEI layer.[23] With a careful choice of carbon precursors, interestingly, we established that the thermal behavior of polymers was responsible for those characteristics, and were able to control electrochemical properties of SnCo alloy embedded carbon nanofibers (CNFs), with or without the long-term capacity fading. This phenomenon has been neither clearly observed in previous studies nor closely investigated as a research subject. This discovery can lead to the new perception of carbon-coated anode design issue for securing long-term electrochemical reliability: the formation mechanism of the SEI layers along the carbon coating and their structural stability in dynamic condition during cycling.

Here, we report a comprehensive study about the influence of morphological evolution of SnCo particles embedded CNFs accompanied with the SEI layer growth on the dimensional stability and electrochemical stabilities. Two carbon precursor polymers, polyvinylpyrrolidone (PVP)[24] and PAN (polyacrylonitrile),[25] were used for the synthesis of the CNFs *via* the electrospinning method. Although both polymers can form complex structures with metal ions[26,27] to assist the formation of homogeneous polymeric fibers,[28] they exhibited different thermal behaviors[29,30] during heat treatment, resulting in contrasting SEI formation/growth and morphological characteristics of CNFs during cycling. To interpret this, we suggest a plausible model explaining the strong correlation between cycleabilities of electrochemical cells and the formation/growth behavior of SEI layers and morphologies of SnCo particles embedded CNFs anode.

RESULTS AND DISCUSSION

Thermal Behavior of Polymers in Synthesis of Carbon Nanofibers Encapsulating SnCo Nanoparticles. The morphological, thermal, and electrochemical properties of polymeric fibers without Sn−Co precursors were shown in Supporting Information Figure S1−S3. In case of synthesizing CNFs, which contain the metallic crystals inside the fiber, the formation of discrete SnCo nanoparticles within CNFs can be significantly affected by thermal behaviors of the polymers during the postcarbonization. Here, we selected two types of polymers, *i.e.*, PVP (1 300 000 g mol^{-1}) and PAN (150 000 g mol^{-1}), to synthesize two different CNFs encapsulating SnCo particles. Although PVP and PAN have similar melting point (∼320 °C), the thermal behaviors of each polymers mixed with metal salt precursors, *i.e.*, Sn^{4+} and Co^{2+}, are markedly different as described in Scheme 1. During the synthesis, as-spun $Sn(OAc)_4$-$Co(OAc)_2$/PVP (hereafter, SnCo/PVP) and $Sn(OAc)_4$-$Co(OAc)_2$/PAN (hereafter, SnCo/PAN) composite fibers were first stabilized in air, and then carbonized in an inert atmosphere to release oxygen and induce carbonization of the polymers. Both PVP and PAN can attract transition metal ions due to

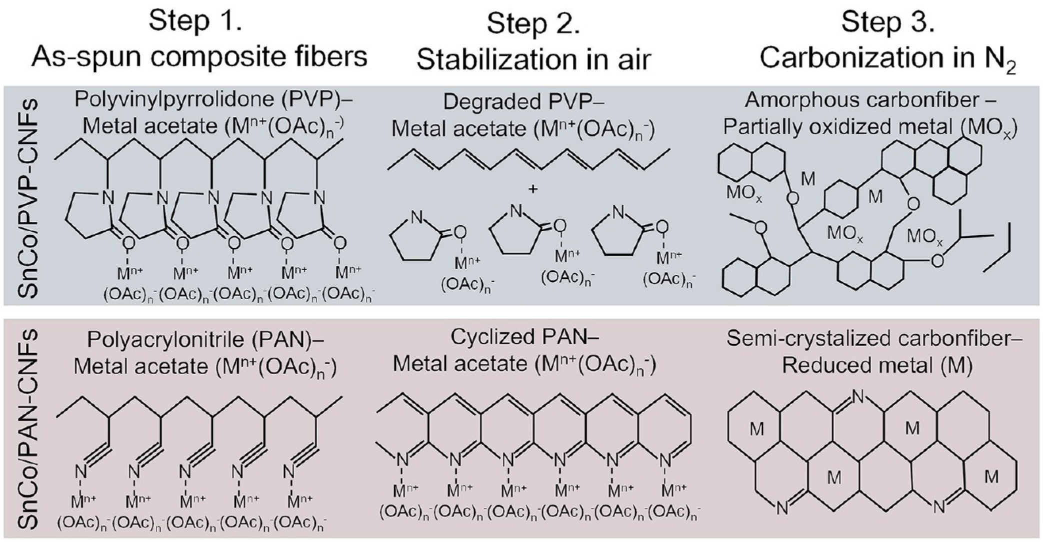

Scheme 1. Schematic illustration of molecular structure transformation of PVP and PAN polymers in the presence of Sn–Co precursors during each heating step.

coordination bond-like interaction between lone pair electrons in oxygen and nitrogen and positively charged metal ions of Sn^{4+} and Co^{2+} dissolved in the solution.[26,27] Therefore, it can help to form homogeneous polymeric as-spun fibers with the presence of metallic ions.[28]

As a result, the as-spun and stabilized SnCo/PVP and SnCo/PAN fibers exhibited smooth morphology without any evidence indicating phase separation between inorganic precursors and polymers (Supporting Information Figure S4).[31] Referring to Scheme 1, the thermal degradation of the initial PVP chains accompanied by the release of pyrrolidone rings takes place with the formation of the vinyl polymers during the stabilization.[32] With increasing temperature up to 300 °C, a double bond in the PVP is formed, thereby reducing the flexibility of fiber matrix followed by formation of intramolecular complexes promoting elimination of the pyrrolidone rings.[29] During the carbonization at 700 °C, it eventually resulted in soft amorphous CNFs caused by depolymerization of linear polymeric chains.[32]

In contrast, PAN includes polar nitrile groups having strong intermolecular interaction, leading to a thermal stability which prevents melting prior to carbonization.[30] In the first stabilization step, the linear PAN molecules are converted to a cyclic structure with repetitive hexagonal ring bridges, which are cross-linked with the metallic ions at the temperature of 250 °C in air.[33,34] These metallic ions, which are interconnected with the cyclic PAN, can reinforce the semicrystalline carbon framework as well as promote homogeneous nucleation of SnCo particles in the CNFs during the carbonization step.

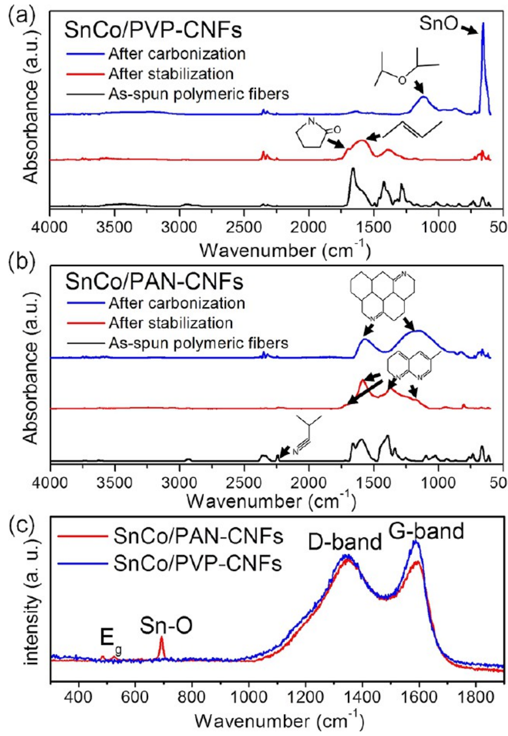

Figure 1. FT-IR spectra of the as-spun, stabilized and carbonized (a) SnCo/PVP-CNFs and (b) SnCo/PAN-CNFs, and (c) Raman spectra of the carbonized SnCo/PVP-CNFs and SnCo/PAN-CNFs.

To clearly verify the phase transformation and the carbonization behaviors of each polymer during the heat treatment, we carried out Fourier transform infrared spectroscopy (FT-IR) and Raman spectra measurements (Figure 1). Panels a and b of Figure 1 show the FT-IR spectra of the SnCo/PVP and the SnCo/PAN after each heat treatment step, respectively. All samples exhibited common fluctuations at 2328 and 2352 cm^{-1}, which were attributed to CO_2 vibration in the experiment chamber. Both as-spun SnCo/PVP and SnCo/PAN showed weak characteristics peaks at 2848 and 2919 cm^{-1}, which were assigned to CH stretch vibration of residual DMF. The common peaks found at

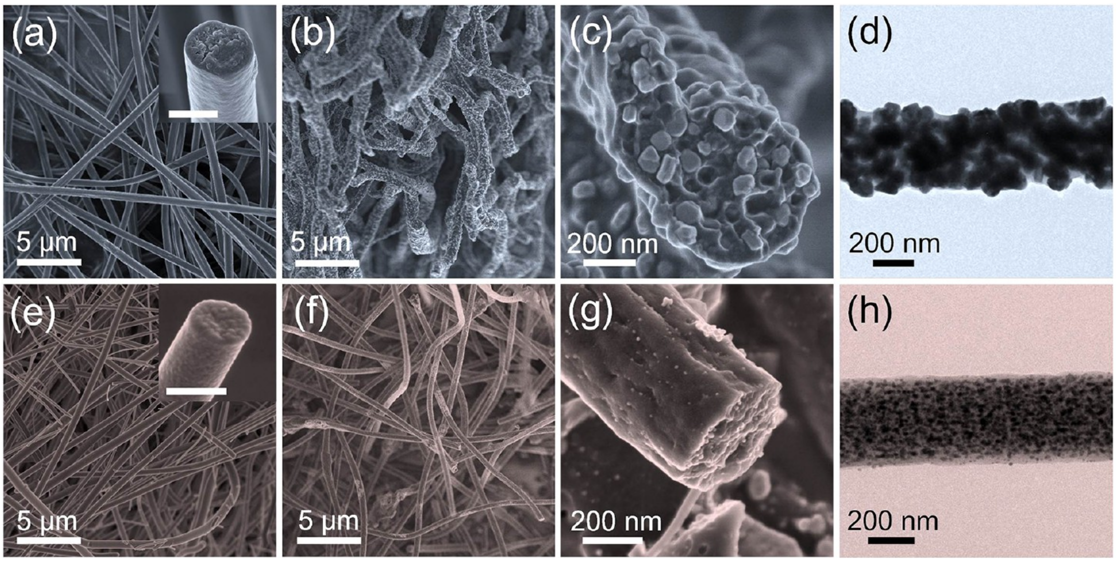

Figure 2. (a) SEM image of stabilized SnCo/PVP, (b and c) SEM images, and (d) TEM image of SnCo/PVP-CNFs. (e) SEM image of stabilized SnCo/PAN, (f and g) SEM images, and (h) TEM image of SnCo/PAN-CNFs. The scale bars in the inset images in (a) and (e) represent 500 nm in length.

1022, 1255, 1371, 1431, and 1660 cm^{-1} indicate the existence of C−O stretching, C−N, $-CH_3$, $-CH_2$, and C−C bondings for DMF and polymer backbones, respectively.[31] The wide absorbance peaks from 1617 to 1592 cm^{-1} indicate C═O stretching vibration for acetate groups.[31] After the stabilization as displayed in Figure 1a, the evolution of wide peak at 1587 cm^{-1} from the SnCo/PVP denotes the conjugated C═C bonds from polymer chains resulting from the release of pyrrolidone ring. At 250 °C, the majority of C−H group is broken down to a new absorption band at 1712 cm^{-1}.[33] Appearance of new shoulder peak at 1720 cm^{-1} is originated from the release of pyrrolidone rings with stretching vibration of C═O.[34] A peak at 1376 cm^{-1} is assigned to C−N bond in pyrrolidone ring. After the carbonization, the peaks corresponding to released pyrrolidone rings and polyethylene polymers disappeared and a new wide peak at 1116 cm^{-1} was observed. This peak corresponds to a C−O−C vibration that is predominantly due to the amorphous carbon consisting small amount of oxygen. A characteristic peak at 657 cm^{-1} is related with Sn−O bond.[35,36]

On the other hand, for the as-spun SnCo/PAN (Figure 1b) fibers, the small peak at 2242 cm^{-1} denoted the nitrile stretch. For the stabilized SnCo/PAN, the nitrile peak was disappeared, and peaks at 1376 and 1592 cm^{-1} are formed, which can correspond to the C−N bond and C═C stretching in the cyclic polymer structure. A small slope at 1716 cm^{-1}, next to the peak corresponding to C−C bonding at 1660 cm^{-1}, indicates C═C bending vibration in the ring structure. After the carbonization, the two wide peaks at 1569 and 1155 cm^{-1} were observed, and they were assigned to C═N and C−N stretching vibrations from the semicrystalline CNFs embedding SnCo particles.[37]

Figure 1c shows Raman spectra of both SnCo particles embedded in the carbonized PVP-driven CNFs and PAN-driven CNFs (hereafter, we denote them as SnCo/PVP-CNFs and SnCo/PAN-CNFs, respectively). In case of the SnCo/PVP-CNFs, the incident laser can be focused on the exposed SnCo particles, and a small fluctuation at 476 cm^{-1} corresponding to E_g mode of oxygen vibration[38] and a peak at 690 cm^{-1} related to the oxidized tin species were identified.[39,40] Considering the D/G ratio of SnCo/PVP-CNFs, SnCo/PVP-CNFs was composed of carbon species with short-range order and multiphase structure.[41] For the SnCo/PAN-CNFs, the peaks indicating the oxidized Sn species are not observed, but a lower D/G ratio of 0.91 was confirmed due to the nature of amorphous carbon species in SnCo/PVP-CNFs with a high graphitic edges density.[41] The Raman results for SnCo/PVP-CNFs also show the presence of the oxidized Sn and the nature of carbon which are in good agreement with the FT-IR spectra and Scheme 1.

Microstructural and Phase Evolution of SnCo Crystallites within Carbon Nanofibers. The morphology and diameter of the stabilized SnCo/PVP fibers exhibited little difference compared to the as-spun ones (Figure 2a). The morphological change of fiber mostly occurred during the carbonization process. After heat treatment at 700 °C in reducing atmosphere, small SnCo alloy particles were observed on the surface of SnCo/PVP-CNFs (Figure 2b). The magnified scanning electron microscopy (SEM) image showed irregular particles with a size distribution of 30−100 nm that were attached to amorphous CNFs (Figure 2c). Figure 2d exhibits a transmission electron microscopy (TEM) image of SnCo/PVP-CNFs. The irregular shape of stuffed SnCo alloy particles was observed on the rough surface as well as inside the fiber structure.

The morphology of SnCo/PVP-CNFs can be considered as an aggregated composite structure comprising SnCo particles covered by amorphous carbon coatings. On the other hand, SnCo/PAN-CNFs did not exhibit exposed SnCo particles but smooth surfaces similar to the stabilized SnCo/PAN as shown in Figure 2e–g. The magnified SEM image in Figure 2g reveals that nanoparticles (<10 nm) are embedded in CNFs having an average diameter of 450 nm. SnCo/PAN-CNFs exhibited the smooth exterior and interior morphologies filled with uniformly distributed nanoparticles with the size distribution of 5–10 nm (Figure 2h). The morphological difference of SnCo alloy particles in each sample can be explained by the different thermal behaviors of the polymers. In the case of the PAN polymer, dense and rigid semicrystalline carbon species were formed, which can prevent outward diffusion of metallic Sn with low melting temperature (231 °C) and abnormal growth of SnCo alloy crystals; thus, single phase SnCo nanoparticles could be uniformly embedded within CNFs. In contrast, the amorphous carbon species obtained from PVP cannot effectively limit the growth of the alloys, inducing large particle formation on the fiber surface, which eventually can lead to inhomogeneous phase evolution.

The crystallization and phase analysis of SnCo alloy were characterized by X-ray diffraction (XRD) patterns, high resolution transmission electron microscopy (HR-TEM), and X-ray photoelectron spectroscopy (XPS) spectra (Figure 3). Figure 3a displays XRD patterns of the SnCo/PVP-CNFs, SnCo/PAN-CNFs, and PDF references of SnO, SnCo, and Co_3Sn_2. The (101), (110), (200), (111), (002), and (201) peaks corresponding to single phase SnCo were observed for both SnCo/PVP-CNFs and SnCo/PAN-CNFs. Slightly broad peaks corresponding to the Co_3Sn_2 and SnO phases were measured for SnCo/PVP-CNFs, which are marked as blue and green arrows, respectively (Figure 3a). In the SnCo/PVP-CNFs, the existence of distinct phases of SnCo, Co_3Sn_2 and SnO were also confirmed by HR-TEM image in Figure 3b and the inset. An optically distinctive phase with a lattice spacing of 0.212 nm also corresponded to (002) planar distance of the SnCo.[42] A lattice spacing of 0.258 nm corresponded to that of (200) planar distance of Co_3Sn_2.[43] The (112) lattice spacing of SnO (0.312 nm) is also in good agreement with the crystallography database (JCPDF no.13-0111).[44] In the SnCo/PVP-CNFs, the (002) lattice spacing of the SnCo alloy particle was measured to be 0.212 nm (Figure 3c).[43] The XPS spectra also confirmed the formation of oxidized SnO species in the SnCo/PVP-CNFs as compared to the existence of purely metallic Sn species in the SnCo/PAN-CNFs (Figure 3d,e). It clearly contrasts the peak intensities between metallic Sn (484.7 eV) and oxidized Sn^{2+} (486.2 eV) species.[45] The phase segregation of heterogeneous SnCo crystallites with multiple phases such as SnO, SnCo, and Co_3Sn_2, as appeared in the SnCo/PVP-CNFs, has been frequently reported elsewhere.[46–48]

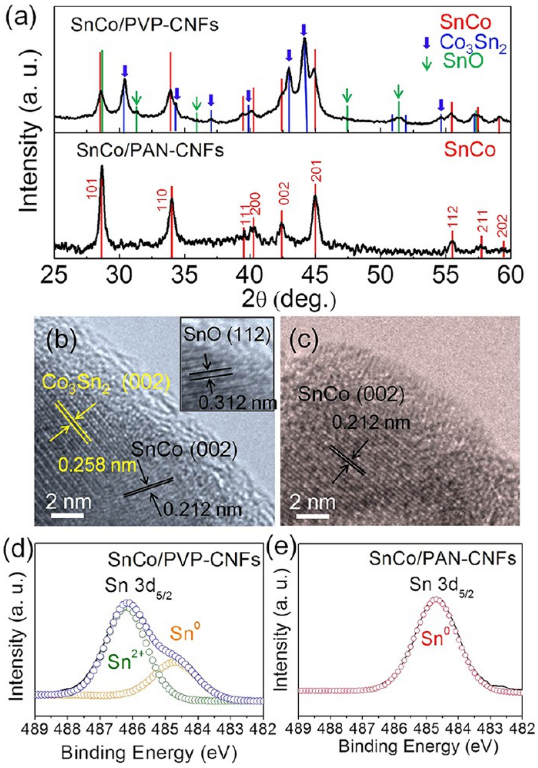

Figure 3. (a) XRD patterns of SnCo/PVP-CNFs (top) and SnCo/PAN-CNFs (bottom). HRTEM images of (b) SnCo/PVP-CNFs and (c) SnCo/PAN-CNFs. X-ray photoelectron spectroscopy (XPS) spectra of (d) SnCo/PVP-CNFs and (e) SnCo/PAN-CNFs.

We conducted a supplementary experiment by varying relative precursor concentrations of Sn (IV) acetate and Co(II) acetate in electrospinning solution in order to investigate the formation of the oxidized species and phase evolution of SnCo crystals in PVP-CNFs (Supporting Information Figure S5). In fact, it suggests that the homogeneous precipitation of single phase SnCo nanocrystals is nearly impossible due to the formation of the oxidized phase, which is induced by oxidation of the metallic ions during the carbonization as proposed in the Scheme 1.

Electrochemical Characterization of Carbon Nanofibers Encapsulating SnCo Particles. To examine the polymer effect on the electrochemical properties, half-cell cycle tests using the SnCo/PAN-CNFs and the SnCo/PVP-CNFs as electrode materials were performed at 0.5 C-rate (Figure 4). The weight portions of Sn in SnCo/PVP-CNFs and SnCo/PAN-CNFs were determined to be 47.45 and 55.75 wt %, respectively, by using element analyzer (EA) and energy-dispersive X-ray spectroscopy (EDS) analyses. The weight of carbon species were calculated by the amount of CO_2 gas arising from the samples in oxygen-rich atmosphere at elevated temperatures. The theoretical capacities of the composite anodes were calculated by considering maximum capacities of Sn (992 mAh/g, with the formation of $Li_{4.4}Sn$ alloy) and CNFs (177 mAh/g).[49] The SnCo/PAN-CNFs exhibited

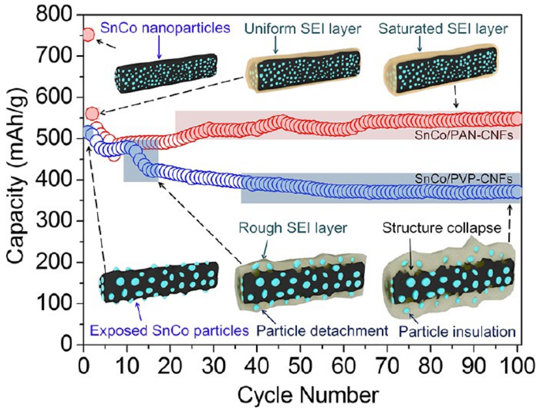

Figure 4. Charge/discharge cycle performance of the SnCo/PVP-CNFs and the SnCo/PAN-CNFs. The cells were cycled between 0.005 and 2.5 V *vs* Li$^+$/Li at the rate of 0.5 C (1 C = 534.4 mAh/g for SnCo/PVP-CNFs and 605 mAh/g for SnCo/PAN-CNFs). The schematic illustrations inside the graph show morphological evolutions of the SnCo/PVP-CNFs and the SnCo/PAN-CNFs in terms of the SEI layer growth and the structure changes.

superior capacity retention of 97.86% from second cycle (560 mAh/g) to 100th cycle (548 mAh/g), which is 90.5% of its theoretical capacity (605 mAh/g). The excellent cyclability can be comparable to the best result of previously reported Sn alloy anodes.[50] In contrast, the SnCo/PVP-CNFs showed a capacity retention of 73.32% from second cycle (506 mAh/g) to 100th cycle (371 mAh/g), which is 69.4% of the theoretical capacity of the SnCo/PVP-CNFs (534.4 mAh/g). Interestingly, the most capacity decrease in the SnCo/PVP-CNFs happened from the 11th to 15th cycle by 52 mAh/g. This characteristic capacity drop was also confirmed in other SnCo/PVP-CNFs samples. One possible explanation would be that large alloy particles loosely attached on amorphous carbon matrix can fall apart from the surface of the CNFs. Therefore, the abrupt capacity drop can takes place due to the electrical contact loss of a certain amount of active mass. The constant decrease in capacity besides the characteristic capacity drop could be resulted from the degradation of amorphous carbon matrix and continuous growth of the SEI films that increase the charge transfer resistance.

The Coulombic efficiencies and both charge/discharge capacities of the SnCo/PVP-CNFs and the SnCo/PAN-CNFs are shown in Figure 5a,b. Whereas the Coulombic efficiencies of the SnCo/PVP-CNFs initially saturated to ~95% up to 12 cycles (Figure 5a), those of the SnCo/PAN-CNFs quickly saturated above 98.7% within 10 cycles (Figure 5b). The reason for the low efficiency of the SnCo/PVP-CNFs at the early cycles should be responsible for activation of exposed particles and irreversible decomposition of electrolyte which had continued at least up to 10 cycles. Although the existence of impurity phases in the SnCo/PVP-CNFs should enhance the cycle performance, the reversibility of charge and discharge is worse than that of SnCo/PAN-CNFs. This is the reason we have focused more on the structural integrity and the SEI growth during charge and discharge cycling. The effect of impurity phase and SnO in electrode performance is described with voltage curves in Supporting Information Figure S6.

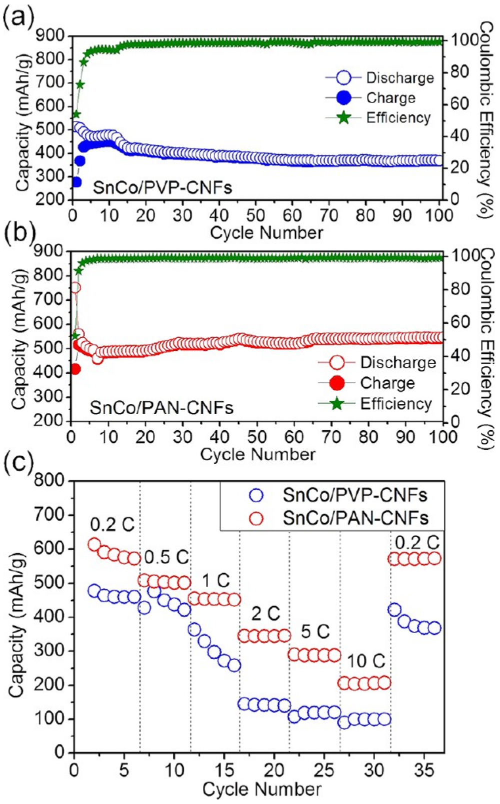

Figure 5. Charge/discharge cycle performances of (a) SnCo/PVP-CNFs and (b) SnCo/PAN-CNFs. The cells were cycled between 0.005 and 2.5 V *vs* Li$^+$/Li at the rate of 0.5 C. (c) Rate capability tests for SnCo/PVP-CNFs and SnCo/PAN-CNFs at rates varied from 0.2 to 10 C (from 2nd cycle to 36th cycle). Each discharge rate was operated with 5 cycle intervals.

The structural instability of amorphous carbon layers combined with high current density can accelerate the collapse of composite structure. The characteristic capacity drop was also observed in the rate capability test with multiple discharge-rate steps from 0.2 to 10 C (Figure 5c). At a discharge rate of 1 C, the decrease in the cycling capacities of the SnCo/PVP-CNFs was accelerated. It can be attributed to the higher internal stress arising from faster lithiation/delithiation of Li$^+$ ions into/out of large Sn alloy particles. It is contrasted to the electrode performance of nanosized SnCo particles in the SnCo/PAN-CNFs: it exhibits very stable capacity retention up to the high discharge rate of 10 C. The capacity at 0.2 C is recovered by almost 100% after the 10 C-rate cycling. The difference in capacity is only 0.2% between the sixth cycle (573.1 mAh/g, 0.2 C) and the 32nd cycle (572.0 mAh/g, 0.2 C).

***Ex Situ* Investigation into the Structure Degradation and SEI Growth during Electrochemical Cycling.** A morphological investigation, as displayed in *ex situ* SEM and TEM

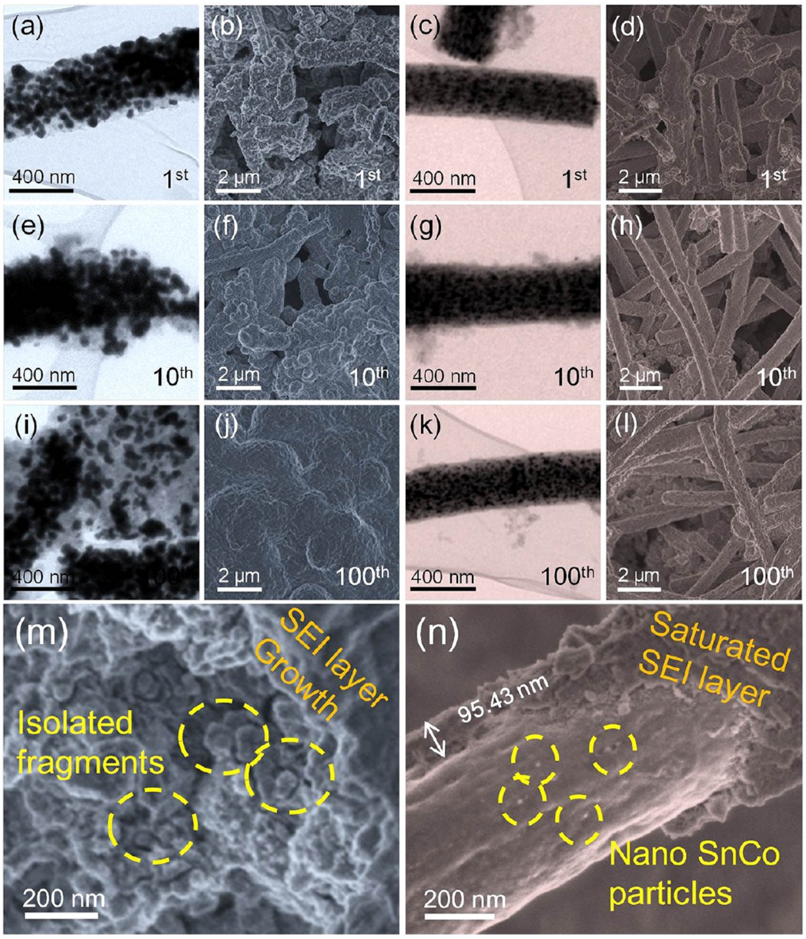

Figure 6. *Ex situ* images of SnCo/PVP-CNFs after 1 cycle: (a) TEM and (b) SEM images. SnCo/PAN-CNFs after 1 cycle: (c) TEM and (d) SEM images. SnCo/PVP after 10 cycles: (e) TEM and (f) SEM images. SnCo/PAN-CNFs after 10 cycles: (g) TEM and (h) SEM images. SnCo/PVP-CNFs after 100 cycles: (i) TEM and (j) SEM images. SnCo/PAN-CNFs after 100 cycles: (k) TEM and (l) SEM images, and magnified *ex situ* SEM images of (m) SnCo/PVP-CNFs and (n) SnCo/PAN-CNFs after 100 cycles.

images of Figure 6, were carried out to confirm that the two polymers as well as the consequent carbon matrix have an important role in securing morphological integrity of anode structures and SEI films. At the first cycle, both the SnCo/PVP-CNFs and SnCo/PAN-CNFs maintained their 1-D shapes that are slightly covered with the SEI layers having noticeable thicknesses. Because large SnCo alloy particles comprising SnCo/PVP-CNFs were loosely anchored on CNFs, irregular surface bumps were clearly observed (Figure 6a). One interesting aspect of the SnCo/PVP-CNFs is the SEI layer formation on the rough surface of fibers (Figure 6b). The SnCo/PAN-CNFs exhibits smooth surface and regular alloy nanoparticles that are perfectly embedded inside the fiber (Figure 6c). The surface morphology of SEI layers is also smooth and uniform throughout the whole composite structure (Figure 6d). After the 10th cycle, we found that a certain portion of SnCo alloy particles of the SnCo/PVP-CNFs was detached from the carbon matrix (Figure 6e). This is in good accordance with the characteristic capacity drop observed in the charge/discharge cycle test. The detached particles are, therefore, proved to be the major cause for the abrupt drop in the capacity of the electrode using SnCo/PVP-CNFs. The roughness and thickness of the SEI layer were intensified by direct observation of SEM images measured at various cycles (Figure 6f). The SnCo/PAN-CNFs, however, shows no difference in morphology to the 10th cycle (Figure 6g,h). In the SnCo/PVP-CNFs, through a series of charge/discharge reactions up to 100 cycles, the loss of active particles and partial degradation of carbon matrix were observed (Figure 6i). The growth rate of the SEI layers was very high so that they covered the whole electrode surface (Figure 6j). To the contrary, the SnCo/PAN-CNFs consistently preserved the fiber and SEI layer morphologies up to the 100th cycle (Figures 6k,l).

To highlight the morphological difference of each fiber, the magnified images of broken sections of SnCo/PVP-CNFs and SnCo/PAN-CNFs after 100 cycles were investigated. Figure 6m reveals that the shattered SnCo particles are randomly dispersed in the chunks of amorphous carbon matrix covered by thick SEI layers without clearly distinguishable CNFs scaffolds. Therefore, the morphological advantages arising from the carbon coating that provides the volume confinement

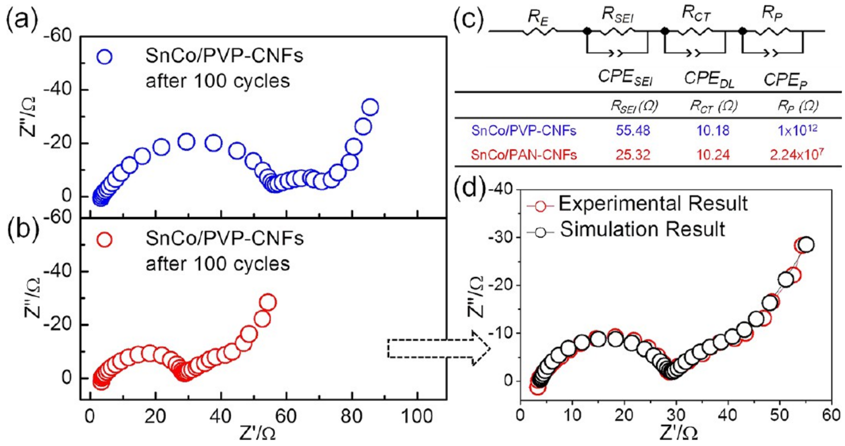

	R_{SEI} (Ω)	R_{CT} (Ω)	R_P (Ω)
SnCo/PVP-CNFs	55.48	10.18	1×10^{12}
SnCo/PAN-CNFs	25.32	10.24	2.24×10^{7}

Figure 7. Nyquist plots of (a) the SnCo/PVP-CNFs (b) and the SnCo/PAN-CNFs half-cells after 100 cycles. (c) The corresponding equivalent circuit and the calculated resistance values of the SnCo/PVP-CNFs and the SnCo/PAN-CNFs. (d) Simulated and measured Nyquist plots using equivalent circuit data from (b).

effect and prevents electrical contact loss of alloy particles became less effective. In addition, the separated SnCo particles from the SnCo/PVP-CNFs can lose their electrical contact by the encapsulation of insulating SEI layers so that the capacity can be noticeably reduced as shown in the cycle test of Figure 4.[48] Furthermore, extensive and continuous volume changes from the exposed particles on fiber surface can lead to exposure of additional fresh particle surfaces followed by the formation of new SEI layers, which reduces the Coulombic efficiencies during cycling.

Meanwhile, the SnCo/PAN-CNFs covered with a uniform and thin SEI layer show that the embedded SnCo nanoparticles are maintained well in terms of their shape and size (Figure 6n), considering the similarity of the fiber morphologies appeared in the TEM images after different number of cycles. All nanoparticles are physically confined in the conductive CNFs so that all the active materials can contribute to the cell capacity.

The additional *ex situ* images including 20th and 50th cycle are provided in the Supporting Information Figure S7. Through the galvanostatic charge/discharge test up to 100th cycle, no specific phase transition was observed by *ex situ* XRD measurements for both SnCo/PVP-CNFs and SnCo/PAN-CNFs (Supporting Information Figure S8). After the first charge/discharge cycle, the crystalline phases of SnCo alloys in both fibers were remained unchanged for the following lithiation/delithation reactions.

To investigate the electrochemical characteristics of the SEI layers, we carried out electrochemical impedance tests. Figure 7 shows the *ex situ* impedance spectra of the SnCo/PVP-CNFs and the SnCo/PAN-CNFs half cells measured after the 100th cycle. Typical three semicircles arranged from high frequency to low frequency were observed in the Nyquist plots.[51] The first semicircle in high frequency range is related to the lithium ion transfer through the SEI layer.[47,51,52] Second and third arcs are in relation with the charge transfer resistance, which is primarily due to the interphase reaction with Li ions and the electrode surface, and phase transformation during Li ion insertion.[53] As shown in Figure 7a,b, the first arc of the SnCo/PVP-CNFs exhibits much larger radius compared to the SnCo/PAN-CNFs. The equivalent circuit for evaluating the difference of impedance result is shown in Figure 7c. R_E represents the ohmic resistance of the cell, R_{SEI} is the SEI layer resistance and R_{CT} and R_P represent the charge transfer resistance and phase transformation resistance, respectively. The parallel capacitances of each resistance factors are presented as constant phase elements (CPE). In the equivalent circuit, CPE_{SEI}, CPE_{DL}, and CPE_P represent the capacitances of the SEI layer, the double layer, and the phase formation, respectively. Considering R_{SEI} values measured in the equivalent circuit, the SnCo/PVP-CNFs (55.48 Ω) showed 2× higher resistance than that (25.32 Ω) of SnCo/PAN-CNFs.

This result demonstrates that the uniformly coated thin SEI layers on the fiber surface of the SnCo/PAN-CNFs provide much less resistance than the thick irregular SEI layers on the SnCo/PVP-CNFs surface. In particular, the extended SEI layers can be created on the surface of detached alloy particles so that the overall R_{SEI} for the SnCo/PVP-CNFs becomes greater than the SnCo/PAN-CNFs. The calculated values in equivalent circuits are simulated to compare with the measured impedance results. All the simulated impedance curves are in good accordance with the measured original values. Figure 7d is an example matching a simulated impedance curve using calculated resistances and CPE values in Figure 7c and the measured impedance curve of the SnCo/PAN-CNFs in Figure 7b. In addition, residual nitrogen species in PAN induced CNFs were measured to 4.2 wt % by EA analysis. The N-doped CNFs can also contribute the superior electrical conductivity[54] compared to PVP-CNFs whose nitrogen composition is only 1.4 wt %.

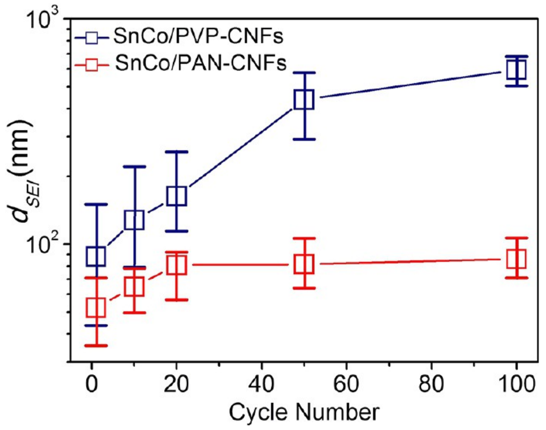

Figure 8. The change in average SEI thicknesses of the SnCo/PVP-CNFs and the SnCo/PAN-CNFs during cycling displayed with error bars.

To quantitatively investigate the growth phenomena of SEI layers on fiber surface along with the cycle number, the thicknesses of SEI layers were measured and collected from the cross sections and the surfaces images. Figure 8 shows the mean thicknesses with max/min bars collected from 10 samples of the SnCo/PVP-CNFs and SnCo/PAN-CNFs. The average SEI layer thickness (d_{SEI}) of the SnCo/PVP after 100 cycles, the average thickness of the SEI layer, reached around 593 nm that is even larger than the original average fiber thickness of 450 nm. For the cycled SnCo/PVP-CNFs, the thicknesses of the SEI layers were mainly estimated by comparing the diameter of the pristine SnCo/PVP-CNFs and the cycled SnCo/PVP-CNFs appeared on the cross-sectional images. Although the accuracy might be not exactly matched to the real value and it may also reflect irreversible dimensional changes during cycling, the dramatic increase in the SEI film thickness of the SnCo/PVP-CNFs is apparent. On the other hand, the SnCo/PAN-CNFs exhibited a steady growth of the SEI layers until the 20th cycle, and the saturated thickness around 90 nm was preserved until the last cycle. The supporting images and statistic data are shown in Supporting Information Figure S9.

Referring to Figure 4 again, the clear contrasts between the SnCo/PVP-CNFs and the SnCo/PAN-CNFs are the particle detachment and the growth of the SEI layers. Even though the impurity phases such as Co_3Sn_2 and SnO should enhance the cycle performance, in SnCo/PVP-CNFs, the reversibility of charge and discharge of SnCo/PVP-CNFs is worse than that of SnCo/PAN-CNFs. As apparently observed in the morphological changes during cycling, the morphological contrast and the corresponding difference in the mechanical stress/strain in the fiber structure played a major role to determine the electrochemical properties of the composite fibers. Some active materials lose physical binding with the SnCo/PVP-CNFs, resulting in detachment of particles that were in turn isolated and insulated by the SEI layers during cycling. The volume change of the exposed alloy particles out of the PVP-driven CNFs can also promote the surface breakage of the SEI layers, so the repeated SEI layer growth can lead to the continuous irreversible capacity loss. Considering the large SEI resistance of the SnCo/PVP-CNFs, the growth of SEI layers with cycling can lead to the decrease in cyclability compared to the case of the SnCo/PAN-CNFs that showed the superior morphological stability with the stable SEI formation owing to the tightly embedded SnCo nanoparticles in rigid CNFs.

Although the active materials used in this experiment are the same, the electrode performance and cyclability are highly contrasted. The significant difference between the cycle performance of the SnCo/PAN-CNFs and SnCo/PVP-CNFs points out that the choice of carbon precursors can play an important role in securing excellent cyclability for 1-D carbon coated metallic particles. To design optimum electrode materials especially for an alloy material which undergoes large volume changes during charge/discharge cycles, we demonstrate that the polymer selection and distribution of active particles within carbon matrix are important factors to determine the performance of electrode.

CONCLUSIONS

In conclusion, we examined the CNFs consisting of SnCo nanoparticles synthesized *via* the electrospinning of two different thermoplastic polymers, PAN and PVP. In contrast to PAN that transformed into the cyclic structure followed by partial crystallization of carbon species during the carbonization step, the linear polymer chains from PVP were thermally degraded, resulting in amorphous carbon matrix that could not limit the agglomeration of SnCo alloys (30–100 nm). Moreover, the residual oxygen in the PVP chains facilitates the partial oxidation of Sn species, while oxygen-free and mechanically robust PAN promotes formation of homogeneous and single phase SnCo nanoparticles (<10 nm). In the electrochemical tests, the SnCo/PVP-CNFs exhibited an abrupt capacity drop around the 10th cycle followed by gradual capacity decreases up to the 100th cycle, which can be explained by the volume-change-induced detachment of the exposed SnCo particles from CNFs and the extended growth of the SEI layers. On the other hand, the SnCo/PAN-CNFs showed higher capacities and better cycle performances. The capacity retention from second cycle to 100th cycle is 97.9% for the SnCo/PAN-CNFs, which is much greater than that (71.9%) of the SnCo/PVP-CNFs. SnCo nanoparticles in the SnCo/PAN-CNFs are neither pulverized nor detached from CNFs so that the SEI thickness is maintained stable after 20 cycles. By encapsulating SnCo nanoparticles in the semicrystalline CNFs, the volume expansion and the particle agglomeration could be effectively prevented. This contrast emphasizes the importance of the carbon precursor as a major factor affecting overall electrode performance of electrospun SnCo-embedded CNFs. The precursor polymer used for deriving the different carbon matrix plays an important role in determination of the particle size and morphology as well as the oxidation of Sn species, thereby affecting the structural stability and the SEI layer growth during electrochemical charge/discharge cycles. Therefore, to design 1-D CNFs anode materials incorporating electrochemically active alloy particles, the carbon precursor has to be carefully considered in terms of its molecular structure and thermal behavior. Possible design factors would be molecular weight, melting point, molecular interaction, the presence of oxygen-rich groups, and the formation of linear *vs* cyclic polymer chains with/without multiple covalent bonds.

METHODS

Synthesis of SnCo/PVP-CNFs and SnCo/PAN-CNFs. Polyvinylpyrrolidone (PVP, 1 300 000 g mol^{-1}) and polyacyrylonitrile (PAN, 150 000 g mol^{-1}) were purchased from Aldrich. Solutions of 6 g of *N*,*N*-dimethylformamide (DMF, Aldrich) containing 7 wt % of PAN powders were prepared by hot stirring at 60 °C. The same solution using PVP was prepared as a comparison. A total of 0.003 mol of Sn (IV) acetate and Co(II) acetate were dissolved into 3 g of DMF. After vigorous stirring for 24 h, the polymer solution (PVP and PAN) were mixed with SnCo precursor solutions. After 48 h of stirring, the blend solutions were sonicated for 5 min to ensure homogeneous mixing. The experiment conditions of electrospinning are as in the following. A 21 gauge stainless steel needle was placed 15 cm above the grounded stainless steel foil collector. A voltage of 15 kV was applied between the needle and the stainless steel foil. A uniform flow rate of 15 μL min^{-1} was maintained by an injection pump. After 12 h to collect as-spun nanofibers mats, the mats were heat treated at 250 °C for 5 h to stabilize polymeric matrix and evaporate residual solvents. After the stabilization, we switched gas in the tube furnace with 20% hydrogen/80% nitrogen mixture gas and increased temperature to 500 °C to promote deoxidation of the SnCo fibers. After forming gas was replaced with pure nitrogen gas (N_2), the temperatures were then increased to 700 °C for 5 h to obtain SnCo/PVP-CNFs and SnCo/PAN-CNFs, respectively. The heating rate was 1 °C min^{-1}.

Materials Characterization. The morphologies of the as-spun polymeric fibers, SnCo/PVP-CNFs, and SnCo/PAN-CNFs were investigated by field-emission scanning electron microscope (FE-SEM, Magellan400, FEI) and field-emission transmission electron microscope (FE-TEM 300KV, Tecnai). To investigate thermal behavior of polymers, Fourier transform infrared spectroscopy measurement (FT-IR, IFS66v/s & Hyperion 3000, Bruker) and Raman spectroscopy (LabRAM HR UV/vis/NIR PL, Horiba Jobin Yvon) were carried out. The formation of SnCo alloy crystals was investigated by X-ray diffraction (XRD, D/MAX-2500 series, RIGAKU) patterns using Cu Kα (λ = 1.54 Å) radiation and high resolution TEM (HRTEM) analysis. The chemical compositions of each fiber were measured by energy-dispersive X-ray spectroscopy (EDS) and element analysis (EA, Flash 2000 series, Thermo Scientific). The oxidation states of Sn were investigated by X-ray photoelectron spectroscopy (XPS, Sigma Probe, Thermo VG Scientific).

Cell Assembly and Electrochemical Characterization. The electrospun SnCo/PVP-CNFs and SnCo/PAN-CNFs were mixed with Super P and polymer binders. Lithium polyacrylate (Li-PAA) was used as a high performance binder material replacing the conventional poly(vinyl difluoride) (PVDF) binder (Supporting Information Figure S10). The ratio to electrospun CNFs, super P, and binder was 75:15:10 in weight. After mixing the components together in 14.474% Li-PAA solution, the obtained black slurry was applied on a Cu foil with a 60 μm-gap applicator followed by overnight vacuum drying at 80 °C. Roll pressing was then carried out after complete removal of the solvent. The obtained SnCo/PVP-CNFs and SnCo/PAN-CNFs composite films coated on the Cu foils were used as working electrodes. A Li foil was used as the counter electrode, and Celgard 2400 was used as the separator. The electrolyte used was 1 M of $LiPF_6$ in ethylene carbonate (EC) and diethyl carbonate (DEC) (1:1 volume ratio). Half-cells were assembled in argon-filled glovebox to 2032 coin cells. Electrochemical cell tests were carried out with a battery cycler (Maccor 4000) at a voltage range between 2.5 and 0.005 V. After cycling tests, the coin cells were discharged to 0.005 V and subsequently used for electrochemical impedance spectroscopy (Si 1260, Solatron) on the frequency range from 100 kHz to 10 mHz with AC voltage amplitude of 5 mV. After the impedance measurement, the coin cells were fully charged (2.5 V) and dissembled in the argon-filled glovebox for *ex situ* SEM, TEM, and XRD analyses.

Conflict of Interest: The authors declare no competing financial interest.

Acknowledgment. This work is supported by the Center for Integrated Smart Sensors funded by the Ministry of Education, Science and Technology as Global Frontier Project (CISS-2012M3A6A6054188). I.-D. Kim acknowledges the support by the Engineering Research Center (ERC-N01120073) program from the Korean National Research Foundation.

Supporting Information Available: Additional SEM images of as-spun fibers; STEM images of SnCo/PVP-CNFs; *ex situ* XRD, TEM, and image analysis data; additional electrochemical data. This material is available free of charge *via* the Internet at http://pubs.acs.org.

REFERENCES AND NOTES

1. Tarascon, J. M.; Armand, M. Issues and Challenges Facing Rechargeable Lithium Batteries. *Nature* **2001**, *414*, 359–367.
2. Winter, M.; Besenhard, J. O.; Spahr, M. E.; Novak, P. Insertion Electrode Materials for Rechargeable Lithium Batteries. *Adv. Mater.* **1998**, *10*, 725–763.
3. Beaulieu, L. Y.; Eberman, K. W.; Turner, R. L.; Krause, L. J.; Dahn, J. R. Colossal Reversible Volume Changes in Lithium Alloys. *Electrochem. Solid-State Lett.* **2001**, *4*, A137–A140.
4. Du, Z.; Zhang, S. Enhanced Electrochemical Performance of Sn Co Nanoarchitectured Electrode for Lithium Ion Batteries. *J. Phys. Chem. C.* **2011**, *115*, 23603–23609.
5. Mao, O.; Turner, R. L.; Courtney, I. A.; Fredericksen, B. D.; Buckett, M. I.; Krause, L. J.; Dahn, J. R. Active/Inactive Nanocomposites as Anodes for Li-Ion Batteries. *Electrochem. Solid-State Lett.* **1999**, *2*, 3–5.
6. Crosnier, O.; Brousse, T.; Schleich, D. M. Tin Based Alloys for Lithium Ion Batteries. *Ionics* **1999**, *5*, 311–315.
7. Mukaibo, H.; Sumi, T.; Yokoshima, T.; Momma, T.; Osaka, T. Electrodeposited Sn-Ni Alloy Film as a High Capacity Anode Material for Lithium-Ion Secondary Batteries. *Electrochem. Solid-State Lett.* **2003**, *6*, A218–A220.
8. Li, H.; Shi, L.; Wang, Q.; Chen, L.; Huang, X. Nano-Alloy Anode for Lithium Ion Batteries. *Solid State Ionics* **2002**, *148*, 247–258.
9. Tamura, N.; Ohshita, R.; Fujimoto, M.; Fujitani, S.; Kamino, M.; Yonezu, I. Study on the Anode Behavior of Sn and Sn−Cu Alloy Thin-Film Electrodes. *J. Power Sources* **2002**, *107*, 48–55.
10. Yin, J.; Wada, M.; Yoshida, S.; Ishihara, K.; Tanase, S.; Sakai, T. New Ag-Sn Alloy Anode Materials for Lithium-Ion Batteries. *J. Electrochem. Soc.* **2003**, *150*, A1129–A1135.
11. Tamura, N.; Kato, Y.; Mikami, A.; Kamino, M.; Matsuta, S.; Fujitani, S. Study on Sn−Co Alloy Anodes for Lithium

Secondary Batteries: I. Amorphous System. *J. Electrochem. Soc.* **2006**, *153*, A1626–A1632.

12. Ferguson, P. P.; Martine, M. L.; George, A. E.; Dahn, J. R. Studies of Tin−Transition Metal−Carbon and Tin−Cobalt−Transition Metal−Carbon Negative Electrode Materials Prepared by Mechanical Attrition. *J. Power Sources* **2009**, *19*, 794–800.
13. Ferguson, P. P.; Dunlap, R. A.; Dahn, J. R. An *in Situ* Study of the Electrochemical Reaction of Li with Nanostructured $Sn_{30}Co_{30}C_{40}$. *J. Electrochem. Soc.* **2010**, *157*, A326–A332.
14. Groult, H.; El Ghallali, H.; Barhoun, A.; Briot, E.; Julien, C. M.; Lantelme, F.; Borensztjan, S. Study of Co−Sn and Ni−Sn Alloys Prepared in Molten Chlorides and Used as Negative Electrode in Rechargeable Lithium Battery. *Electrochim. Acta* **2011**, *56*, 2656–2664.
15. Zhang, W. M.; Wu, X. L.; Hu, J. S.; Guo, Y. G.; Wan, L. J. Carbon Coated Fe_3O_4 Nanospindles as a Superior Anode Material for Lithium-Ion Batteries. *Adv. Funct. Mater.* **2008**, *18*, 3941–3946.
16. Ng, S. H.; Wang, J.; Wexler, D.; Konstantinov, K.; Guo, Z. P.; Liu, H. K. Highly Reversible Lithium Storage in Spheroidal Carbon-Coated Silicon Nanocomposites as Anodes for Lithium-Ion Batteries. *Angew. Chem., Int. Ed.* **2006**, *45*, 6896–6899.
17. Aurbach, D.; Ein-Eli, Y.; Chusid, O.; Carmeli, Y.; Babai, M.; Yamin, H. The Correlation between the Surface Chemistry and the Performance of Li-Carbon Intercalation Anodes for Rechargeable 'Rocking-Chair' Type Batteries. *J. Electrochem. Soc.* **1994**, *141*, 603–611.
18. Jung, Y. S.; Lee, K. T.; Oh, S. M. Si−Carbon Core−Shell Composite Anode in Lithium Secondary Batteries. *Electrochim. Acta* **2007**, *52*, 7061–7067.
19. Kim, S. P.; van Duin, A. C. T.; Shenoy, V. B. Effect of Electrolytes on the Structure and Evolution of the Solid Electrolyte Interphase (SEI) in Li-ion Batteries: A molecular Dynamics Study. *J. Power Sources* **2011**, *196*, 8590–8597.
20. Hwang, T. H.; Lee, Y. M.; Kong, B. S.; Seo, J. S.; Choi, J. W. Electrospun Core−Shell Fibers for Robust Silicon Nanoparticle-Based Lithium Ion Battery Anodes. *Nano Lett.* **2012**, *12*, 802–807.
21. Chan, C. K.; Peng, H.; Liu, G.; McIlwrath, K.; Zhang, X. F.; Huggins, R. A.; Cui, Y. High-Performance Lithium Battery Anodes Using Silicon Nanowires. *Nat. Nanotechnol.* **2008**, *3*, 31–35.
22. Bhattacharya, S.; Alpas, A. T. Micromechanisms of Solid Electrolyte Interphase Formation on Electrochemically Cycled Graphite Electrodes in Lithium-ion Cells. *Carbon.* **2012**, *50*, 5359–5357.
23. Wu, H.; *et al.* Stable Cycling of Double-Walled Silicon Nanotube Battery Anodes through Solid-Electrolyte Interphase Control. *Nat. Nanotechnol.* **2012**, *7*, 310–315.
24. Wang, P.; Zhang, D.; Ma, F.; Ou, Y.; Chen, N. Q.; Xieb, S.; Li, J. Mesoporous Carbon Nanofibers with a High Surface Area Electrospun from Thermoplastic Polyvinylpyrrolidone. *Nanoscale* **2012**, *4*, 7199–7204.
25. Yu, Y.; Gu, L.; Wang, C.; Dhanabalan, A.; van Aken, P. A.; Maier, J. Encapsulation of Sn@Carbon Nanoparticles in Bamboo-Like Hollow Carbon Nanofibers as an Anode Material in Lithium-Based Batteries. *Angew. Chem., Int. Ed.* **2009**, *48*, 6485–6489.
26. Liu, M.; Yan, X.; Liu, H.; Yu, W. An Investigation of the Interaction between Polyvinylpyrrolidone and Metal Cations. *React. Funct. Polym.* **2000**, *44*, 55–64.
27. Zhang, Z.; Zhang, L.; Wang, S.; Chen, W.; Lei, Y. A Convenient Route to Polyacrylonitrile/Silver Nanoparticle Composite by Simultaneous Polymerization-Reduction Approach. *Polymer* **2001**, *42*, 8315–8318.
28. Choi, S. H.; Hwang, I. S.; Lee, J. H.; Oha, S. G.; Kim, I. D. Microstructural Control and Selective C_2H_5OH Sensing Properties of Zn_2SnO_4 Nanofibers Prepared by Electrospinning. *Chem. Commun.* **2011**, *47*, 9315–9317.
29. Bogatyrev, V. M.; Borisenko, N. V.; Pokrovskii, V. A. Thermal Degradation of Polyvinylpyrrolidone on the Surface of Pyrogenic Silica. *Russ. J. Appl. Chem.* **2001**, *74*, 814–819.
30. Huang, X. Fabrication and Properties of Carbon Fibers. *Materials* **2009**, *2*, 2369–2430.
31. Shin, J.; Choi, S. J.; Lee, I.; Youn, D. Y.; Park, C. O.; Lee, J. H.; Tuller, H. L.; Kim, I. D. Thin-Wall Assembled SnO_2 Fibers Functionalized by Catalytic Pt Nanoparticles and Their Superior Exhaled-Breath-Sensing Properties for the Diagnosis of Diabetes. *Adv. Funct. Mater.* **2013**, *23*, 2357–2367.
32. Peniche, C.; Zaldivar, D.; Pazos, M.; Paz, S.; Bulay, A.; Roman, J. S. Study of the Thermal Degradation of Poly(N-vinyl-2-pyrrolidone) by Thermogravimetry−FTIR. *J. Appl. Polym. Sci.* **1993**, *50*, 485–493.
33. Raymundo-Pinero, E.; Cazorla-Amoros, D.; Linares-Solano, A. The Role of Different Nitrogen Functional Groups on the Removal of SO_2 from Flue Gases by N-doped Activated Carbon Powders and Fibres. *Carbon* **2003**, *41*, 1925–1932.
34. Nakanishi, K. *Infrared Absorption Spectroscopy*; Nankido: Tokyo, 1962.
35. Kim, Y. I.; Moon, H. S.; Ji, K. S.; Seong, S. H.; Park, J. W. SnO_2 Thin Film Doped with Si for Negative Electrode of Microbattery in MEMS. *J. Korean Phys. Soc.* **2001**, *39*, S337–S340.
36. Ristic, M.; Ivanda, M.; Popovic, S.; Music, S. Dependence of Nanocrystalline SnO_2 Particle Size on Synthesis Route. *J. Non-Cryst. Solids* **2002**, *303*, 270–280.
37. Guo, J.; Yang, Z.; Yu, Y.; Abruna, H. D.; Archer, L. A. Lithium−Sulfur Battery Cathode Enabled by Lithium−Nitrile Interaction. *J. Am. Chem. Soc.* **2013**, *135*, 763–767.
38. Gontia, I. I.; Baibarac, M.; Baltog, I. Photoluminescence and Raman Studies on Tin Dioxide Powder and Tin Dioxide/Single-Walled Carbon-nanotube Composites. *Phys. Status Solidi B* **2011**, *248*, 1494–1498.
39. Wu, Q. H.; Song, J.; Lia, J. High Oxygen Vacancy Tin Oxide Synthesized by Combustion Chemical Vapor Deposition (CCVD). *Surf. Interface Anal.* **2008**, *40*, 1488–1492.
40. Sun, S. H.; Meng, G. W.; Zhang, G. X.; Gao, T.; Geng, B. Y.; Zhang, L. D.; Zuo, J. Raman Scattering Study of Rutile SnO_2 Nanobelts Synthesized by Thermal Evaporation of Sn Powders. *Chem. Phys. Lett.* **2003**, *376*, 103–107.
41. Kong, F.; Kostecki, R.; Nadeau, G.; Song, X.; Zagnib, K.; Kinoshita, K.; McLarnon, F. *In Situ* Study of SEI Formation. *J. Power Sources* **2001**, *97*−*98*, 58–66.
42. Li, M. Y.; Liu, C. L.; Shi, M. R.; Dong, W. S. Nanostructure Sn−Co−C Composite Lithium Ion Battery Electrode with Unique Stability and High Electrochemical Performance. *Electrochim. Acta* **2011**, *56*, 3023–3028.
43. Di, L. M.; Zhou, G. F.; Bakker, H. Atomic Disorder, Phase Transformation, and Phase Restoration in Co_3Sn_2. *Phys. Rev. B* **1993**, *47*, 4890–4895.
44. JCPDF Card No.13-0111.
45. Szuber, J.; Czempik, G.; Larciprete, R.; Koziej, D.; Adamowicz, B. XPS Study of the L-CVD Deposited SnO_2 Thin Films Exposed to Oxygen and Hydrogen. *Thin Solid Films* **2001**, *391*, 198–203.
46. Cui, W.; Wang, F.; Wang, J.; Wang, C.; Xia, Y. Nanostructural CoSnC Anode Prepared by $CoSnO_3$ with Improved Cyclability for High-Performance Li-ion Batteries. *Electrochim. Acta* **2011**, *56*, 4812–4818.
47. Lavela, P.; Nacimiento, F.; Ortiz, G. F.; Tirado, J. L. Sn−Co−C Composites Obtained from Resorcinol-Formaldehyde Gel as Anodes in Lithium-ion Batteries. *J. Solid State Electrochem.* **2010**, *14*, 139–148.
48. Li, M. Y.; Liu, C. L.; Shi, M. R.; Dong, W. S. Nanostructure Sn−Co−C Composite Lithium Ion Battery Electrode with Unique Stability and High Electrochemical Performance. *Electrochim. Acta* **2011**, *56*, 3023–3028.
49. Ryu, W. H.; Shin, J.; Jung, J. W.; Kim, I. D. Cobalt(II) Monoxide Nanoparticles Embedded in Porous Carbon Nanofibers as a Highly Reversible Conversion Reaction Anode for Li-Ion Batteries. *J. Mater. Chem. A* **2013**, *1*, 3239–3243.
50. Kamali, A. R.; Fray, D. J. Tin-Based Materials as Advanced Anode Materials for Lithium Ion Batteries: A Review. *Rev. Adv. Mater. Sci.* **2011**, *27*, 14–24.
51. Yang, C. R.; Song, J. Y.; Wang, Y. Y.; Wan, C. C. Impedance Spectroscopic Study for the Initiation of Passive Film on Carbon Electrodes in Lithium Ion Batteries. *J. Appl. Electrochem.* **2000**, *30*, 29–34.

52. Barsoukov, E.; Kim, J. H.; Kim, J. H.; Yoon, C. O.; Lee, H. Effect of Low-Temperature Conditions on Passive Layer Growth on Li Intercalation Materials *In Situ* Impedance Study. *J. Electrochem. Soc.* **1998**, *145*, 2711–2717.
53. Xue, L. J.; Xu, Y. F.; Huang, L.; Ke, F. S.; He, Y.; Wang, Y. X.; Wei, G. Z.; Li, J. T.; Sun, S. G. Lithium Storage Performance and Interfacial Processes of Three Dimensional Porous Sn−Co Alloy Electrodes for Lithium-Ion Batteries. *Electrochim. Acta* **2011**, *56*, 5979–5987.
54. Ismagilov, Z. R.; *et al.* Structure and Electrical Conductivity of Nitrogen-Doped Carbon Nanofibers. *Carbon* **2009**, *47*, 1922–1929.